Journal of Materials Chemistry C

Towards a Better Understanding of the Forming and Resistive Switching Behavior of Ti-Doped HfOx RRAM

Journal:	*Journal of Materials Chemistry C*
Manuscript ID	TC-ART-10-2021-004734.R2
Article Type:	Paper
Date Submitted by the Author:	03-Mar-2022
Complete List of Authors:	Athena, Fabia Farlin; Georgia Institute of Technology College of Engineering, Electrical and computer engineering West, Matthew; Georgia Institute of Technology, School of Materials Science and Engineering Hah, Jinho; Georgia Institute of Technology College of Engineering, Materials Science and Engineering; Georgia Institute of Technology Hanus, Riley; Georgia Institute of Technology College of Engineering, 3George W. Woodruff School of Mechanical Engineering, Georgia Institute of Technology, Atlanta, Georgia 30332, USA Graham, Samuel; Georgia Institute of Technology College of Engineering, George W. Woodruff School of Mechanical Engineering, Georgia Institute of Technology, Atlanta, Georgia 30332, USA Vogel, Eric; Georgia Institute of Technology, Materials Science and Engineering

Towards a Better Understanding of the Forming and Resistive Switching Behavior of Ti-Doped HfO_x RRAM

Fabia F. Athena[1], Matthew P. West[2], Jinho Hah[2], Riley Hanus[3], Samuel Graham[2,3], and Eric M. Vogel[1,2*]

[1]School of Electrical and Computer Engineering, Georgia Institute of Technology, Atlanta, Georgia 30332, USA

[2]School of Materials Science and Engineering, Georgia Institute of Technology, Atlanta, Georgia 30332, USA

[3]George W. Woodruff School of Mechanical Engineering, Georgia Institute of Technology, Atlanta, Georgia 30332, USA

[*]Email: eric.vogel@mse.gatech.edu

ABSTRACT: HfO_x-based resistive random-access memory (RRAM) devices are being widely considered as both non-volatile memories for digital computation and synaptic memory for neuromorphic computing applications. The resistive switching mechanism in these materials is known to be highly dependent on the presence of oxygen vacancies and other dopants. In this work, HfO_x is doped with titanium using sequential atomic layer deposition (ALD) of HfO_x and TiO_x. An increase in the titanium dopant content results in a decrease of the forming voltage, a decrease of both allowable set and reset stop voltages, and a decrease of the high resistance state (HRS) of the RRAM. The physical mechanisms responsible for these observed behaviors are proposed.

KEYWORDS: *RRAM, Ti doping, charge-to-breakdown, HfO_x, XPS depth profile, sub-oxide.*

1. INTRODUCTION

Memristors have recently gained widespread attention because of their potential in both non-volatile memory (NVM) and brain-inspired computing applications.[1, 2] Brain-inspired computing is an emerging field to circumvent the bottlenecks associated with traditional von Neumann

architectures where data storage and processing are separate.[3-8] This architecture limits the speed of operations such as matrix-vector multiplication, which are critical when performing complex artificial intelligence (AI) tasks, such as speech and pattern recognition. Studies have shown that memristors can be integrated into neuromorphic circuits to circumvent this bottleneck by performing data storage and processing on the same physical component.[9-11] Among recently proposed brain-inspired devices[2, 12], anion migration-based metal oxide filamentary devices, also known as Valence Change Mechanism (VCM) devices, have received widespread attention. Although cation-based RRAM have consistently shown higher on/off ratios, VCM devices have other advantages such as higher endurance, improved retention, and lower power consumption.[13, 14] However, the mechanisms driving VCM memristor operation remains elusive.[1, 15, 16]

Among recently reported binary oxides (e.g., Al_2O_3, NiO, TiO_2, TaO_2, ZrO_2, HfO_2), HfO_x has been a primary focus due to several promising features including: CMOS compatibility, scalability (<10 nm), fast writing speed (<1 ns), good switching endurance (>10^{10} cycles), and lower energy consumption. [17-19] Within the adaptive oxide layer of a filamentary memristor, a conductive filament is formed through a dielectric breakdown process. Subsequently, this conductive filament is partially ruptured and reformed during the set and reset operations which controls the resistance state of the device. Therefore, the chemistry of the active layer is expected to be critically important to memristor function. The activation energy for defect (e.g., oxygen vacancies) motion in the active layer is critical in determining the nonlinear switching dynamics.[3]

One approach that impacts the defect (e.g., vacancies) activation energy and initial concentration is the addition of dopants.[20] Improved resistive switching (RS) behavior for doped

transition metal oxide-based RRAM devices has been shown by previous studies.[21-24] Incorporation of Cu dopants into MoO_x/GdO_x bilayer-based filamentary devices has led to significant improvements in device performance such as improved reproducibility and long-term state retention.[25] Another previous study reported that oxygen vacancies (V_o) can be added to HfO_x through S doping resulting in device improvement such as more uniformity in resistance change and stable endurance.[26] In addition, an increase of oxygen vacancy (V_o) defect concentration in the active layer has been shown to lead to enhanced switching characteristics such as stable multi-level resistive switching, a higher on/off ratio, and gradual reset behvaior.[27] Al-doped HfO_x based devices along with post-deposition annealing have been shown to have promising multi-level switching characteristics.[28-30] Studies have shown that aliovalent ion doping via sputtering into HfO_x-based devices have better uniformity of the low resistance state (LRS) and high resistance state (HRS) due to increased concentration of non-lattice oxygen.[28, 31] Moreover, there have been previous studies on the impact of titanium doping in HfO_x memristors with the active materials synthesized via sputtering. For example, devices containing a sputtered $HfO_x/TiO_x/HfO_x/TiO_x$ multilayer (ML) have shown multilevel capability and analog reset characteristics.[32, 33] The addition of a titanium metallic interlayer at the HfO_x active layer in sputtered HfO_x RRAM devices has been shown to produce uniform set and reset switching.[32, 34] However, sputtered oxides have properties different than ALD deposited oxides[35, 36] and ALD deposited oxides are more suitable for industrial RRAM applications.[37] One previous study used ALD to synthesize titanium doped HfO_x memristors and demonstrated multi-level resistive switching capabilities.[38] However, a top titanium capping layer was not used, which has proven beneficial for RRAM such as lowering the forming voltage and improving the switching window and device yield[19, 39] and a detailed understanding of the impact of titanium doping on forming and switching was not been reported.

In this work, RRAM devices, with amorphous $Hf_xTi_yO_z$ synthesized using sequential ALD, were fabricated. The results suggest that the observed reduction in forming voltage with increasing titanium doping content in the active layer is due to both an increase in the tunnel current and an increase in the rate of defect generation as a function of titanium concentration. Following forming, the resistive switching characteristics show a decrease in the HRS as a function of titanium doping concentration in the active layer. XPS results suggest that this is likely due to an increase in available electronic states with increasing titanium. It should be noted that as all the devices have the Ti capping layer, therefore, no changes are derived from the capping layer.

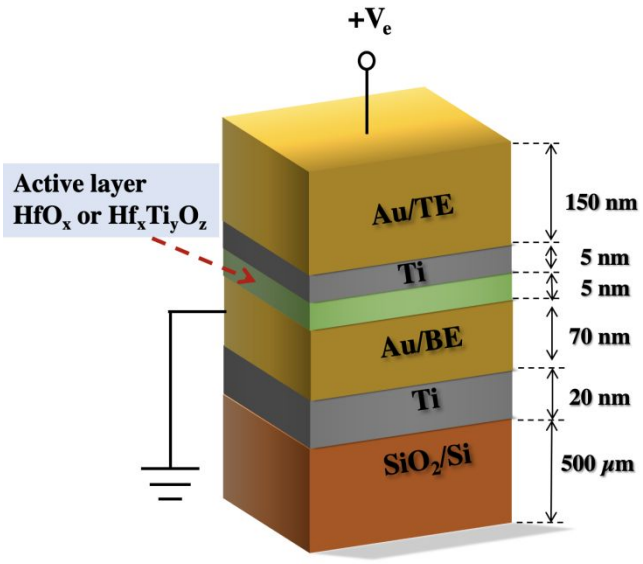

Figure 1. A schematic of the device stack with layer thicknesses indicated.

2. EXPERIMENTAL METHODS

RRAM devices with amorphous HfO_x and $Hf_xTi_yO_z$ with varying Hf:Ti ratios were fabricated. Figure 1 shows a schematic of the fabricated device structure. Bottom Au electrodes (~70 nm)

were deposited using electron beam evaporation and patterned using mask-less lithography on a silicon wafer having 310 nm of SiO_2. The adaptive oxides were deposited using thermal atomic layer deposition (ALD) at 250 ˚C. The sequence consisted of repeating a number of cycles of tetrakis (dimethylamido) hafnium (TDMAHf) + deionized water, followed by a number of cycles of tetrakis (dimethylamido) titanium (TDMAT)+ deionized water for the total number of sequences (~50) necessary to achieve a ~5 nm film. Four conditions were used: pure HfO_x, Hf:Ti = 3:1, Hf:Ti = 2:1, and Hf:Ti = 1:1. Following ALD, a 5 nm Ti capping layer was deposited by electron beam evaporation, immediately followed by ~150 nm of Au as the top electrode (TE) without breaking vacuum. An O_2 plasma descum (500 sccm, 30 sec, plasma power 150 W) process was performed before each deposition step to ensure the removal of the photoresist and increase device yield. Our standard 30 sec descum process did not impact the oxidation state of Au significantly (Figure S1). A separate set of control samples were also synthesized along with the devices consisting of the (~ 5 nm) adaptive oxides deposited on Si/SiO_2 substrates.

X-ray photoelectron spectroscopy (XPS) was performed using a monochromatic Al K-alpha X-ray source ($h\upsilon$ = 1486.6 eV), 400 μm spot size, and 15 W X-ray gun power. For XPS depth profiles, Ar^+ sputtering was performed at an incident angle of 30˚ and a low energy of 1 KeV ion energy to avoid preferential sputtering.[40] To correct for surface potential variation associated with charging, the C 1s peak at 285.0 eV was used as the reference energy. The XPS spectra were fit using a Shirley background[41] and Lorentzian–Gaussian (GL 30) line shapes.

A Keithley 4200 semiconductor analyzer [42] was used for the electrical measurements. The devices were formed by sweeping the voltage of the top electrode at a current compliance of 0.1 mA. After forming, incremental reset voltages were applied (gradual reset process) from 0 V to the

maximum achievable negative voltage. This step was followed by the application of 30 hysteresis loops to defined set and reset stop voltage parameters. Charge-to-breakdown (Q_{BD}) measurements of the devices were performed using the constant-voltage stress (CVS) method.[43, 44] Integration of the measured current as a function of stress time was used to determine the Q_{BD}.

3. RESULTS AND DISCUSSIONS

3.1 XPS Characterization: X-ray photoelectron spectroscopy (XPS) was performed to quantify the active layer stoichiometry. XPS depth profiles of the relative atomic ratios of Hf, Ti, and O have been calculated as shown in Figure S2. The Hf:Ti ALD pulsing ratios of 3:1, 2:1, 1:1 resulted in approximate Hf:Ti elemental ratios of 3.14:1, 2.3:1, and 1.14:1, respectively (Figure S1). Detailed stoichiometric analysis of $Hf_xTi_yO_z$ for all oxide samples are provided in the supplementary section (Figure S3). The ratios were calculated from the average elemental ratios at the surface and the first etch level. The results demonstrate successful doping of the HfO_x matrix with titanium. These results suggest that while the HfO_x and TiO_x layers were pulsed sequentially, the resulting oxide layer is well mixed. Individual XPS depth profile result is shown in Figure S4 for all sample types. Figure 2 illustrates the relationship between the bonded oxygen content and titanium concentration. A linear decrease of the bonded-oxygen content with an increase in titanium concentration was observed.

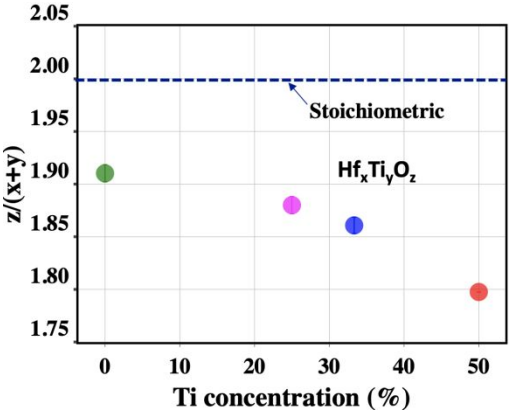

Figure 2. XPS analysis of the oxides (HfO_x and $Hf_xTi_yO_z$) used in the active layer of the devices. z/(x+y) value of $Hf_xTi_yO_z$ (bonded oxygen content) as a function of titanium concentration. Bonded oxygen content decreases for the higher titanium doped samples. This indicates an increase of the non-stoichiometry with an increase of titanium content.

3.2 Forming Characteristics: Figure 3(a) shows the typical current-voltage characteristics obtained during forming. Figure 3(b) shows that the current at a given voltage increases exponentially with increasing titanium content. Figure 3(c) shows that the voltage required to achieve filament formation (forming voltage) decreases with increasing titanium content. There are several likely reasons for this reduction in forming voltage with increasing titanium content. The generation of defects in oxides is known to be proportional to electron fluence.[45] Prior to forming, the current flowing through the oxide increases exponentially with increasing titanium content resulting in increasing defect generation at the lower voltage. We hypothesize that the tunnel current in Ti-doped sample is increasing with increasing titanium concentration because of a decrease in the metal to oxide barrier height as TiO_2 has smaller bandgap; the bandgap of amorphous HfO_2 and TiO_2 are 6.0 eV and 3.1 eV, respectively.[46, 47] Moreover, prior work on ALD titanium doped HfO_x has independently measured the barrier height and observed a similar trend.[48] Whether one is considering direct tunneling or trap assisted tunneling, the current density is exponentially dependent on the barrier height. Fitting of the experimental current-voltage characteristic with both the trap-assisted and direct tunneling models (Figure S5) suggests that the conduction mechanism is likely trap-assisted. Second, the initial, as-deposited, defect concentration (e.g., oxygen vacancies, V_0) is likely higher in the oxides with higher titanium content. As the bonded oxygen amount (z) decreases with titanium content (Figure 2(b)), fewer defects must be generated to cause

run-away filament formation. Furthermore, the rate of defect generation at a given voltage during forming may be higher with increased titanium content. To further explore whether titanium doping is impacting the defect generation probability, detailed constant voltage dielectric breakdown experiments have been conducted.

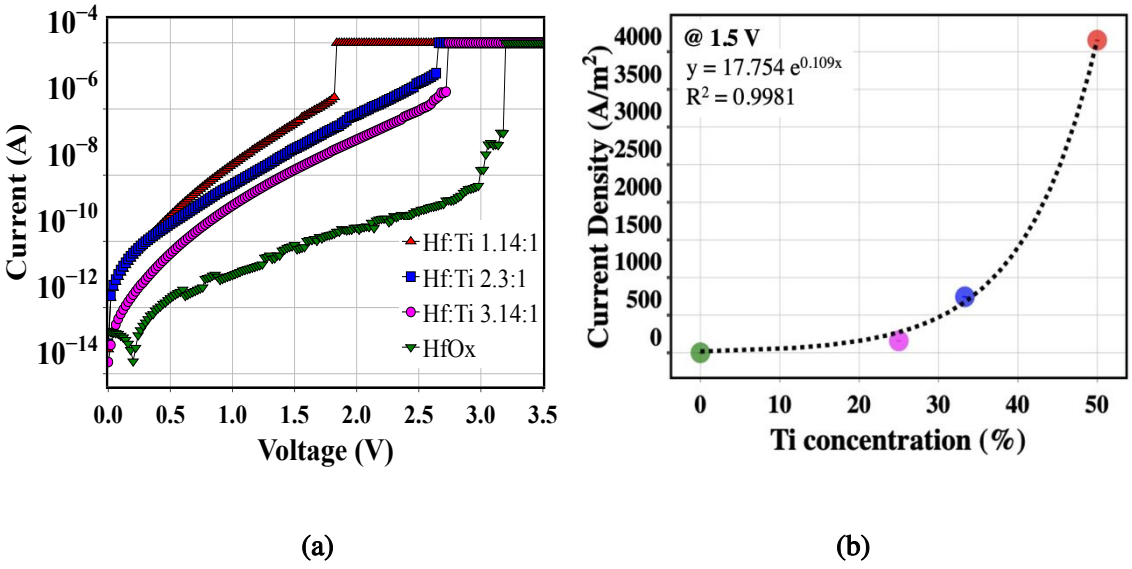

Figure 3. Forming characteristics of HfO_x and $Hf_xTi_yO_z$ devices. (a) Example current-voltage relationships for the devices with varying titanium concentration, (b) Current density as a function of titanium concentration at 1.5 V during forming. An exponential increase of the measured current is observed with increasing titanium concentration. (c) Statistical analysis of forming voltages. All data sets are statistically analyzed based on 20 devices of each oxide sample. Here, the green triangle is average, the box top edge indicates 75th percentile, the box bottom edge indicates 25th percentile, the top bar is maximum, the bottom bar is minimum, and the middle line is median.

3.3 Breakdown Measurements:

Figure 4 (a) shows the average charge-to-breakdown characteristics as a function of voltage at room temperature for HfO_x and $Hf_xTi_yO_z$ (e.g., 3.14:1 and 1.14:1) devices. The dotted line is an exponential fit as a function of voltage. The statistical distributions used to obtain the average Q_{BD} are shown in Figure S5. The extrapolation of the charge-to-breakdown at a given voltage indicates that for the same voltage, the Q_{BD} decreases exponentially with increasing titanium content which is shown in Figure 4 (b). For instance, at 2.7 V the Q_{BD} for the pure HfO_x device is approximately two orders of magnitude higher compared to the device having a Hf:Ti ratio of 3.14:1.

The charge-to-breakdown (Q_{BD}) is known to be proportional to the number of generated defects required to initiate breakdown (N^{BD}) and inversely proportional to the defect generation rate (P_g),[44, 49, 50]

$$Q_{BD} \propto \frac{N^{BD}}{P_g}$$

There are two possible reasons for the observed decrease in Q_{BD} with increasing titanium content. First, there are wide variety of reasons that can cause an increase in the number of pre-existing defects with titanium concentration which could reduce the number of generated defects necessary to initiate filament formation (N^{BD}). One possible reason is the magnitude of the molar Gibbs free energy for vacancy formation in HfO_2 (-1088.2 eV) is higher than TiO_2 (-888.8 eV).[19] This is consistent with a reduction in bonded oxygen (increasing oxygen vacancies) with increasing titanium concentration as observed in Figure 2(b). However, this reduction in bonded oxygen is observed to be approximately linear with increasing titanium concentration. Therefore, while there may be a linear decrease in N_{BD} with increasing titanium concentration, this likely does not explain an exponential decrease in Q_{BD}.

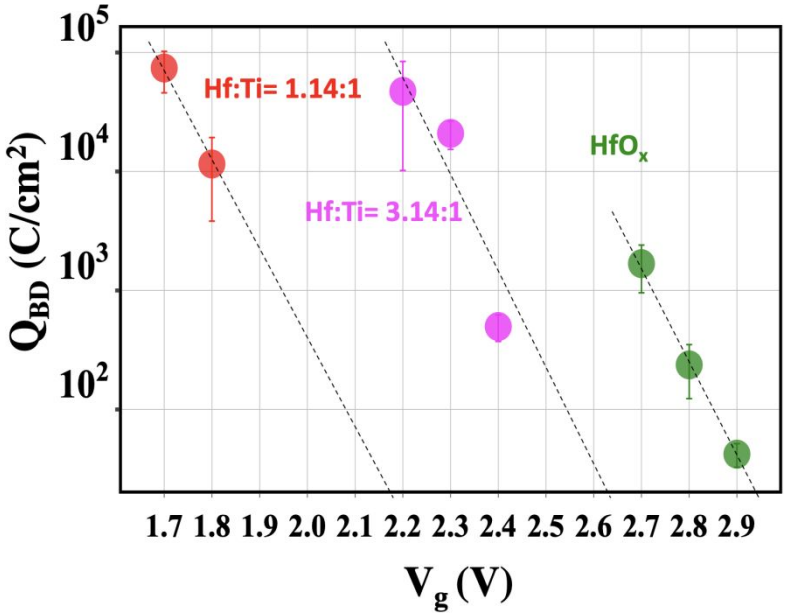
10^5
10^4
10^3
10^2
Q_{BD} (C/cm^2)
Hf:Ti= 1.14:1
Hf:Ti= 3.14:1
HfO_x
1.7 1.8 1.9 2.0 2.1 2.2 2.3 2.4 2.5 2.6 2.7 2.8 2.9
V_g (V)

(a)

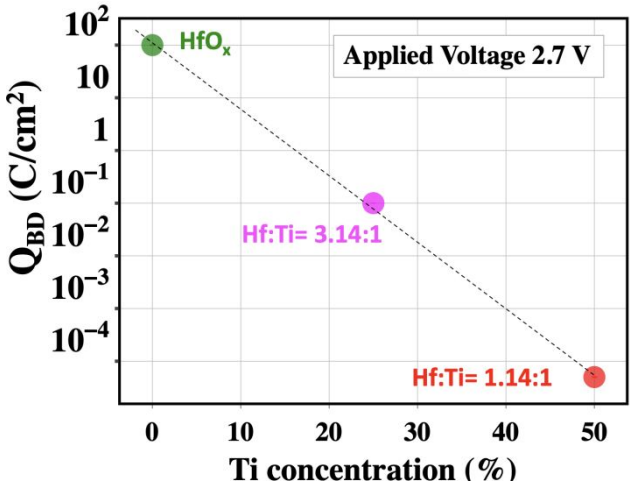
10^2
10
1
10^{-1}
10^{-2}
10^{-3}
10^{-4}
Q_{BD} (C/cm^2)
HfO_x
Applied Voltage 2.7 V
Hf:Ti= 3.14:1
Hf:Ti= 1.14:1
0 10 20 30 40 50
Ti concentration (%)

(b)

Figure 4. Breakdown measurement of HfO_x and $Hf_xTi_yO_z$ devices. (a) Measured (average) charge-to-breakdown as a function of gate voltage (V_g) at room temperature. For a given voltage, charge-to-breakdown exponentially decreases with the increase of titanium concentration. (b) Charge to breakdown (Q_{BD}) at a given voltage (2.7 V) as a function of titanium content. The charge to breakdown (Q_{BD}) indicates that for the same voltage (e.g., for this case 2.7 V) charge to breakdown (Q_{BD}) decreases exponentially with increasing titanium content. Here y axes are in the logarithmic scale. Weibull distributions and examples of current-time relationships are shown in Figure S6 and S7.

The second, and more likely, reason for an exponential decrease in Q_{BD} with increasing titanium concentration is that the rate of defect generation (P_g) at a given voltage increases exponentially with increasing titanium concentration. Ab-initio calculations suggest that the energy for defect formation in titanium-doped amorphous HfO_2 (2.1 eV) is less than that of pure HfO_2 (2.9 eV).[51] The rate of defect generation is expected to be exponentially dependent on this activation energy[52] explaining the observed Q_{BD} behavior.

3.4 Switching Dynamics: After forming, the performed gradual reset processes (explained in the methods section) and the following hysteresis loops to stabilize the filament are shown in Figure S8. Figure 5(a) shows typical hysteresis loops after stabilization for each of the oxides. As shown in Figure 5(b), the maximum set and reset stop voltages that can be applied to the device without causing permanent breakdown depend on the titanium content. As shown in Figure 6(a), this causes the switching window, which is the ratio of the HRS to LRS, to decrease with increasing titanium content.

Although the addition of titanium reduces the forming voltage, the devices with large titanium concentration (Hf:Ti = 2:3, 1:1) also show a reduced switching window. For the devices with Hf:Ti=3.1:1, the forming voltage is 25% smaller than the HfO_x devices; however, the switching

window is comparable. Therefore, the Hf:Ti=3.1:1 devices provide an optimum trade-off between forming voltage and switching window.

As observed in Figure 6(b), the decrease in switching window with increasing titanium content is primarily due to a decrease in the high resistance state (HRS); the low resistance state (LRS) is approximately independent of the titanium content.

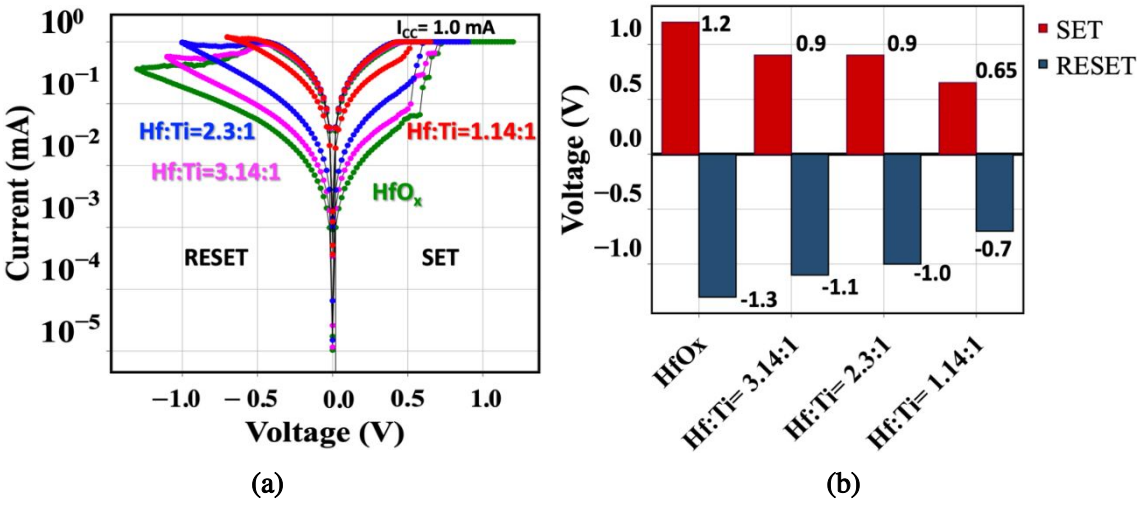

Figure 5. Current-voltage relationships of the devices during switching. (a) DC bipolar I-V sweeping loops with the application of maximum set and reset stop voltages, (b) applied set and reset stop voltages. The higher Ti-doped devices show higher current in the reset side. Maximum applicable set and reset stop voltages decreases with the increase of titanium content in the device.

It is possible that the change in the HRS with titanium content is due to the lower voltages used in the set and reset with increasing titanium content. To determine if this is the case, Figure 7(a) shows the hysteresis loops performed on each of the oxides using the same set and reset stop voltage of +0.65 V and -0.70 V, respectively. Figure 7(b) shows that for the same set and reset stop voltage conditions, the HRS still decreases with increasing titanium content. This phenomenon suggests that the difference in HRS is related to the titanium, not the measurement condition. Moreover, the HRS is independent of the device area, implying that the current is flowing through the filament.[53]

The HRS (low current) state is impacted by the change of active-layer material doping. The filament is known to be partially oxidized during reset resulting in a lower current than the LRS.[54]

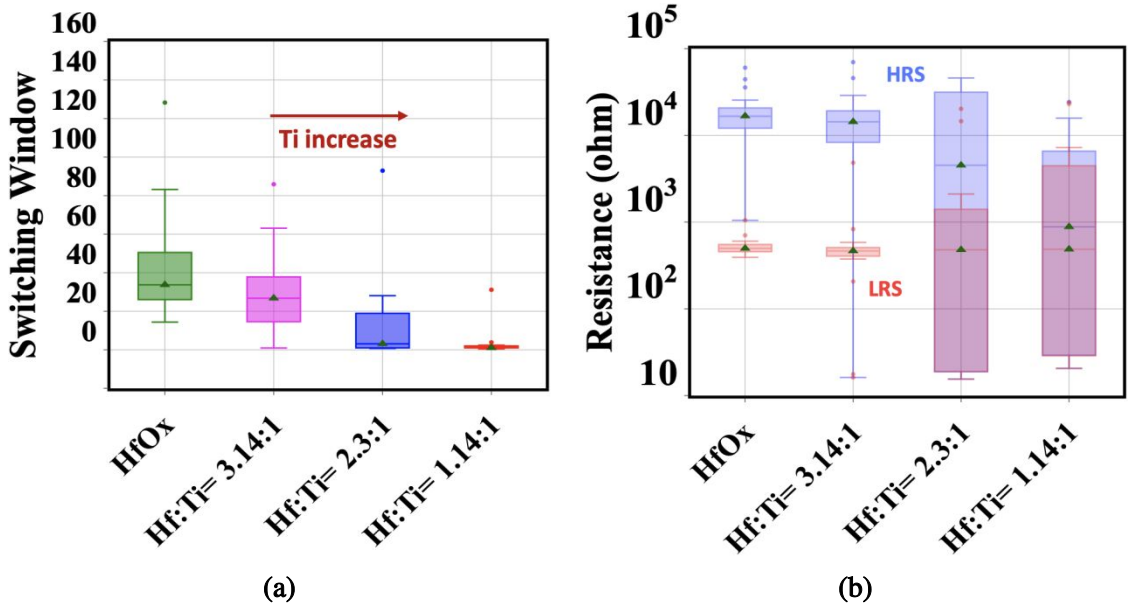

Figure 6. The statistical distribution of the switching characteristics of the devices. (a) Switching window, (b) LRS and HRS. HRS decreases while LRS stays constant with the increase of titanium content. The switching window decreases with the increase of titanium content. The decrease of the switching window is mainly because of the decrease of HRS with titanium doping. All data sets are statistically analyzed based on 20 devices of each oxide sample. Here, the green triangle is average, the box top edge indicates 75th percentile, the box bottom edge indicates 25th percentile, the top bar is maximum, the bottom bar is minimum, and the middle line is median.

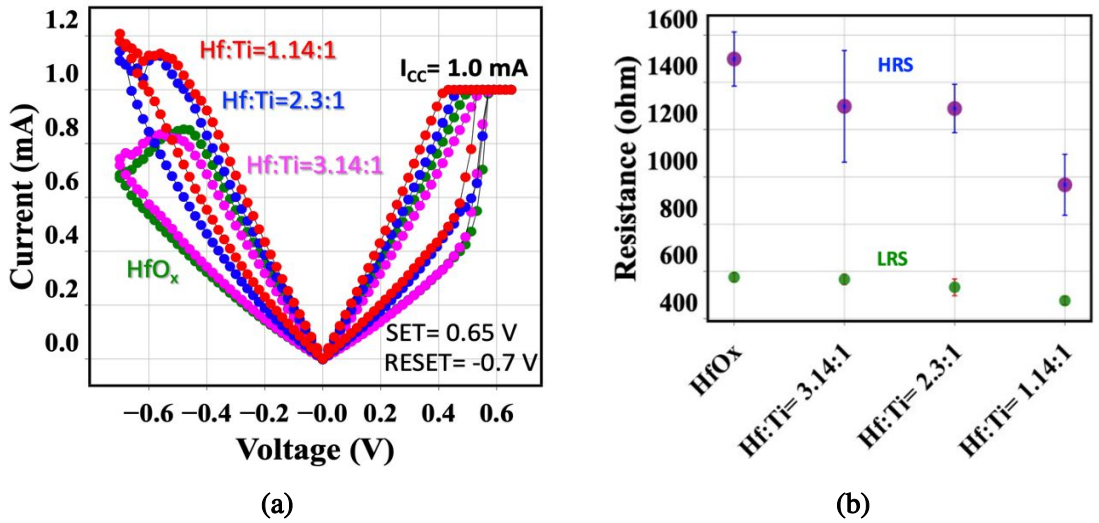

Figure 7. The observed switching characteristics with the application of the same SET (0.65 V) and RESET (-0.75 V) stop voltages on HfO_x and $Hf_xTi_yO_z$ samples. (a) The characteristic current-voltage relationships of the devices with 1 mA current compliance. The switching window decreases as the titanium dopant in the device increases, (b) LRS and HRS distribution. Even for the same set and reset stop voltages, HRS decreases, and LRS stays constant for devices with higher titanium concentration.

Moreover, it has been observed that with the increase of titanium doping in HfO_x, the amount of suboxide (TiO_x, where $1 \leq x < 2$) and metallic titanium increases. Here, suboxide translates to any sub-stoichiometric TiO_x component that has lower amount of oxygen bonded to titanium metal relative to stoichiometric TiO_2. These suboxide states have been shown to have electronic states near the Fermi edge resulting in increased conductivity with increasing titanium content.[55]

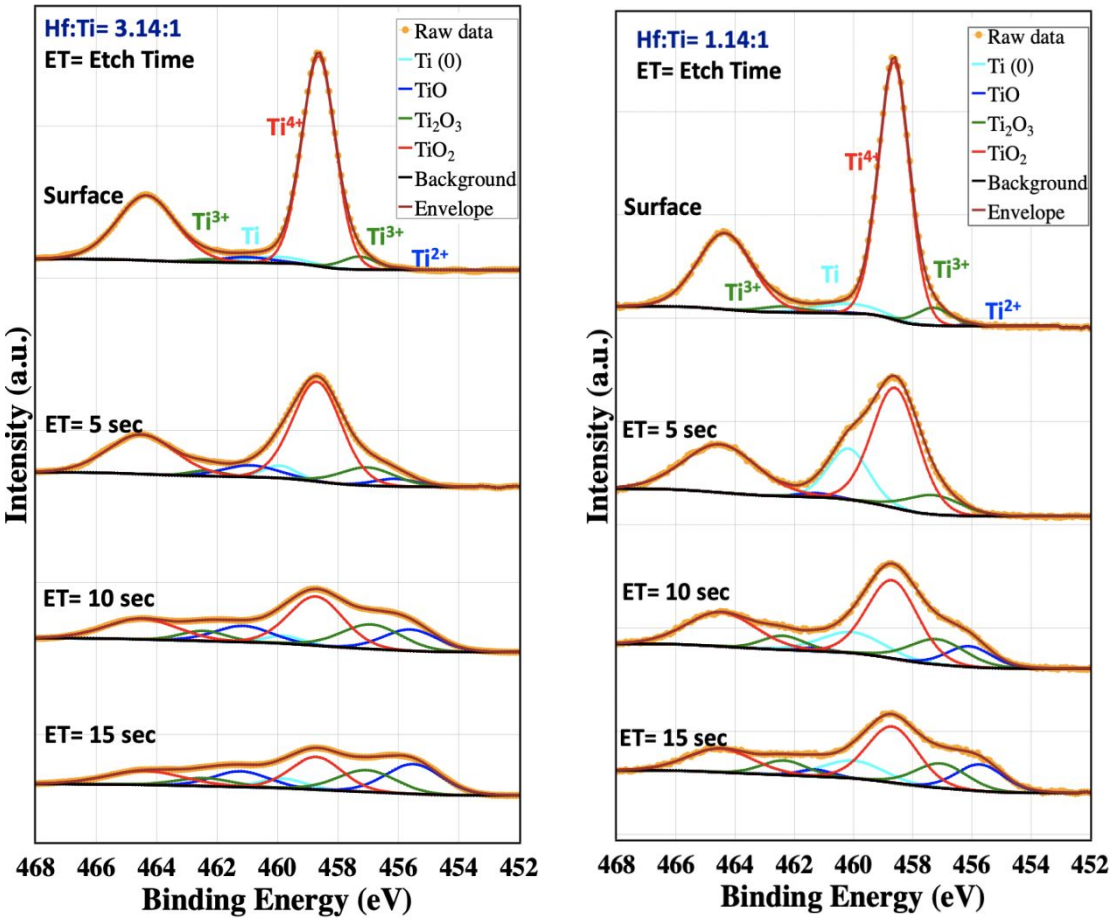

(a) (b)

Figure 8. Deconvolution of the Ti XPS peaks. (a) Hf:Ti = 3.14:1, (b) Hf:Ti = 1.14:1. The concentration of Ti sub-oxides and the metallic titanium content are higher in the Hf:Ti = 1.14:1 sample compared to the Hf:Ti = 3.14:1 sample.

To explore this possibility, the Ti 2p peaks from the XPS depth profile of titanium-doped samples (Hf:Ti = 3.14:1 and Hf:Ti = 1.14:1) have been deconvoluted as shown in Figure 8(a) and Figure 8(b). Quantitative analysis of the Ti 2p peak deconvolution[56] are provided in the supplementary information (Table S3). It is apparent that the metallic titanium and suboxide contents are relatively higher for the more heavily titanium-doped samples. For instance, at etch time 5 seconds, the Ti peak is higher for 1.14:1 sample compared to the 3.14:1 sample. The presence of a higher amount of metallic titanium and suboxides results in increased conductivity for heavily titanium-doped samples because of increased available electronic states. This causes a decrease in HRS with the increase of titanium content. In the LRS, the current flow through the metallized filament would be weakly dependent on the titanium content and the conduction is mainly ohmic. Therefore, the LRS is approximately independent of the titanium content.

4. CONCLUSIONS

HfO_x and titanium-doped HfO_x (Hf:Ti= 3.14:1, 2.3:1, 1.14:1) RRAM devices have been fabricated to uncover the materials defect chemistry that drives forming and switching behavior. The forming voltage decreases and current increases with increasing titanium content. This is due to the combined effects of a higher tunnel current (caused by decreased barrier height), higher initial defect concentration and higher probability of defect formation during forming. Detailed charge-to-breakdown experiment suggests that an exponential decrease of breakdown charge (Q_{BD}) with

the increase of titanium content is mainly caused by the increase of defect formation probability. After forming, the HRS is observed to decrease with increasing titanium, whereas the LRS is constant, even for the same set and reset stop voltages. XPS results suggest that this is likely due to an increase in available electronic states or defect-induced charge carriers in the oxide. The LRS is not impacted by the addition of titanium as the conductivity of the metallic filament is weakly dependent on the titanium content. Overall, the results provide a fundamental understanding of the impact of titanium doping on the forming and switching behavior of HfO_x-based RRAM. Investigating the effect of doping on switching characters of HfO_2 devices may help to improve their performance that makes this study relevant to current technology needs. As the forming and resistive switching operation causes creation and stabilization of the filament, respectively, are also crucial for analog switching of a filamentary memory. Analyzing the impact of titanium doping on analog neuromorphic behavior is also important to better understand synaptic response; this is the focus of future work.

SUPPLYMENTARY MATERIAL

See supplementary material for the additional information.

ACKNOWLEDGMENTS:

This work was supported by the Air Force Office of Scientific Research MURI entitled, “Cross-disciplinary Electronic-ionic Research Enabling Biologically Realistic Autonomous Learning (CEREBRAL)” under Award No. FA9550-18-1-0024. This work was performed in part at the Georgia Tech Institute for Electronics and Nanotechnology, a member of the National Nanotechnology Coordinated Infrastructure (NNCI), which is supported by the National Science

Foundation (No. ECCS-2025462). This material is based upon the work supported by the Georgia Tech ECE Fellowship and National Science Foundation Graduate Research Fellowship under Grant No. DGE- 1650044.

CONFLICT OF INTERESTS: Authors declare no conflict of interests.

FINANCIAL IERESTS: Authors declare no financial interests.

References

1.Sun, W.; Gao, B.; Chi, M.; Xia, Q.; Yang, J. J.; Qian, H.; Wu, H., Understanding memristive switching via in situ characterization and device modeling. *Nature communications* **2019,** *10* (1), 1-13.

2.Zhang, Y.; Wang, Z.; Zhu, J.; Yang, Y.; Rao, M.; Song, W.; Zhuo, Y.; Zhang, X.; Cui, M.; Shen, L., Brain-inspired computing with memristors: Challenges in devices, circuits, and systems. *Applied Physics Reviews* **2020,** *7* (1), 011308.

3.Yang, J. J.; Strukov, D. B.; Stewart, D. R., Memristive devices for computing. *Nature nanotechnology* **2013,** *8* (1), 13-24.

4.Sebastian, A.; Le Gallo, M.; Khaddam-Aljameh, R.; Eleftheriou, E., Memory devices and applications for in-memory computing. *Nature nanotechnology* **2020,** *15* (7), 529-544.

5.Zhu, J.; Zhang, T.; Yang, Y.; Huang, R., A comprehensive review on emerging artificial neuromorphic devices. *Applied Physics Reviews* **2020,** *7* (1), 011312.

6.Zidan, M. A.; Strachan, J. P.; Lu, W. D., The future of electronics based on memristive systems. *Nature electronics* **2018,** *1* (1), 22-29.

7.Ielmini, D.; Wong, H.-S. P., In-memory computing with resistive switching devices. *Nature Electronics* **2018,** *1* (6), 333-343.

8.Wong, H.-S. P.; Salahuddin, S., Memory leads the way to better computing. *Nature nanotechnology* **2015,** *10* (3), 191-194.

9.Strukov, D.; Indiveri, G.; Grollier, J.; Fusi, S., Building brain-inspired computing. *Nature Communications* **2019,** *10* (1).

10.Yu, Z.; Abdulghani, A. M.; Zahid, A.; Heidari, H.; Imran, M. A.; Abbasi, Q. H., An Overview of Neuromorphic Computing for Artificial Intelligence Enabled Hardware-Based Hopfield Neural Network. *IEEE Access* **2020,** *8*, 67085-67099.

11.Jeong, H.; Shi, L., Memristor devices for neural networks. *Journal of Physics D: Applied Physics* **2018,** *52* (2), 023003.

12.Zhang, T.; Yang, K.; Xu, X.; Cai, Y.; Yang, Y.; Huang, R., Memristive Devices and Networks for Brain-Inspired Computing. *physica status solidi (RRL)–Rapid Research Letters* **2019,** *13* (8), 1900029.

13.Lu, A.; Peng, X.; Li, W.; Jiang, H.; Yu, S., NeuroSim Simulator for Compute-in-Memory Hardware Accelerator: Validation and Benchmark. *Frontiers in Artificial Intelligence* **2021,** *4*.

14.Chou, C.-C.; Lin, Z.-J.; Tseng, P.-L.; Li, C.-F.; Chang, C.-Y.; Chen, W.-C.; Chih, Y.-D.; Chang, T.-Y. J. In *An N40 256K× 44 embedded RRAM macro with SL-precharge SA and low-voltage current limiter to improve read and write performance*, 2018 IEEE International Solid-State Circuits Conference-(ISSCC), IEEE: 2018; pp 478-480.

15.Yang, R.; Huang, H. M.; Guo, X., Memristive synapses and neurons for bioinspired computing. *Advanced Electronic Materials* **2019,** *5* (9), 1900287.

16.Chen, J. Y.; Huang, C. W.; Chiu, C. H.; Huang, Y. T.; Wu, W. W., Switching kinetic of VCM-based memristor: evolution and positioning of nanofilament. *Advanced Materials* **2015,** *27* (34), 5028-5033.

17.Wong, H.-S. P.; Lee, H.-Y.; Yu, S.; Chen, Y.-S.; Wu, Y.; Chen, P.-S.; Lee, B.; Chen, F. T.; Tsai, M.-J., Metal–oxide RRAM. *Proceedings of the IEEE* **2012,** *100* (6), 1951-1970.

18.Basnet, P.; Pahinkar, D. G.; West, M. P.; Perini, C. J.; Graham, S.; Vogel, E. M., Substrate dependent resistive switching in amorphous-HfO_x memristors: An experimental and computational investigation. *Journal of Materials Chemistry C* **2020,** *8* (15), 5092-5101.

19.Wang, X. P.; Chen, Y. Y.; Pantisano, L.; Goux, L.; Jurczak, M.; Groeseneken, G.; Wouters, D. In *Effect of anodic interface layers on the unipolar switching of HfO_2-based resistive RAM*,

Proceedings of 2010 International Symposium on VLSI Technology, System and Application, IEEE: 2010; pp 140-141.
20.Pornprasertsuk, R.; Ramanarayanan, P.; Musgrave, C. B.; Prinz, F. B., Predicting ionic conductivity of solid oxide fuel cell electrolyte from first principles. *Journal of applied physics* **2005,** *98* (10), 103513.
21.Tsunoda, K.; Kinoshita, K.; Noshiro, H.; Yamazaki, Y.; Iizuka, T.; Ito, Y.; Takahashi, A.; Okano, A.; Sato, Y.; Fukano, T. In *Low power and high speed switching of Ti-doped NiO ReRAM under the unipolar voltage source of less than 3 V*, 2007 IEEE International Electron Devices Meeting, IEEE: 2007; pp 767-770.
22.Lin, C.-C.; Tu, B.-C.; Lin, C.-H.; Tseng, T.-Y., Resistive Switching Mechanisms of V-Doped $SrZrO_3$ Memory Films. *IEEE electron device letters* **2006,** *27* (9), 725-727.
23.Guan, W.; Long, S.; Liu, Q.; Liu, M.; Wang, W., Nonpolar nonvolatile resistive switching in Cu doped ZrO_2. *IEEE Electron Device Letters* **2008,** *29* (5), 434-437.
24.Lv, H.; Wan, H.; Tang, T., Improvement of resistive switching uniformity by introducing a thin GST interface layer. *IEEE electron device letters* **2010,** *31* (9), 978-980.
25.Yoon, J.; Choi, H.; Lee, D.; Park, J.-B.; Lee, J.; Seong, D.-J.; Ju, Y.; Chang, M.; Jung, S.; Hwang, H., Excellent Switching Uniformity of Cu-Doped MoO_x/GdO_x Bilayer for Nonvolatile Memory Applications. *IEEE electron device letters* **2009,** *30* (5), 457-459.
26.Zhang, Z.; Wang, F.; Hu, K.; She, Y.; Song, S.; Song, Z.; Zhang, K., Improvement of Resistive Switching Performance in Sulfur-Doped HfO_x-Based RRAM. *Materials* **2021,** *14* (12), 3330.
27.Zhang, H.; Gao, B.; Sun, B.; Chen, G.; Zeng, L.; Liu, L.; Liu, X.; Lu, J.; Han, R.; Kang, J., Ionic doping effect in ZrO_2 resistive switching memory. *Applied Physics Letters* **2010,** *96* (12), 123502.
28.Roy, S.; Niu, G.; Wang, Q.; Wang, Y.; Zhang, Y.; Wu, H.; Zhai, S.; Shi, P.; Song, S.; Song, Z., Toward a reliable synaptic simulation using Al-Doped HfO_2 RRAM. *ACS applied materials & interfaces* **2020,** *12* (9), 10648-10656.
29.Peng, C.-S.; Chang, W.-Y.; Lee, Y.-H.; Lin, M.-H.; Chen, F.; Tsai, M.-J., Improvement of resistive switching stability of HfO_2 films with Al doping by atomic layer deposition. *Electrochemical and Solid State Letters* **2012,** *15* (4), H88.
30.Congedo, G.; Wiemer, C.; Lamperti, A.; Cianci, E.; Molle, A.; Volpe, F. G.; Spiga, S., Atomic layer-deposited Al–HfO_2/SiO_2 bi-layers towards 3D charge trapping non-volatile memory. *Thin Solid Films* **2013,** *533*, 9-14.
31.Lee, K.; Kim, Y.; Na, H.; Sohn, H., Effect of aliovalent impurities on the resistance switching characteristics of sputtered hafnium oxide films. *Journal of Vacuum Science & Technology B, Nanotechnology and Microelectronics: Materials, Processing, Measurement, and Phenomena* **2015,** *33* (3), 032204.
32.Yu, S.; Gao, B.; Fang, Z.; Yu, H.; Kang, J.; Wong, H. S. P., A low energy oxide-based electronic synaptic device for neuromorphic visual systems with tolerance to device variation. *Advanced Materials* **2013,** *25* (12), 1774-1779.
33.Fang, Z.; Yu, H.; Li, X.; Singh, N.; Lo, G.; Kwong, D., $HfO_x/TiO_x/HfO_x/TiO_x$ Multilayer-Based Forming-Free RRAM Devices With Excellent Uniformity. *IEEE Electron Device Letters* **2011,** *32* (4), 566-568.
34.Lee, D.; Sung, Y.; Lee, I.; Kim, J.; Sohn, H.; Ko, D.-H., Enhanced bipolar resistive switching of HfO_2 with a Ti interlayer. *Applied Physics A* **2011,** *102* (4), 997-1001.
35.Ahn, J.; Lee, J. Y.; Kim, J.; Yoo, J.; Ryu, C. In *Comparison study from sputtering, sol-gel, and ALD processes developing embedded thin film capacitors*, 2006 8th Electronics Packaging Technology Conference, IEEE: 2006; pp 10-14.
36.Johnson, R. W.; Hultqvist, A.; Bent, S. F., A brief review of atomic layer deposition: from fundamentals to applications. *Materials today* **2014,** *17* (5), 236-246.

37.Ritala, M.; Niinistö, J., Industrial applications of atomic layer deposition. *ECS transactions* **2009,** *25* (8), 641.
38.Chakrabarti, B.; Galatage, R. V.; Vogel, E. M., Multilevel Switching in Forming-Free Resistive Memory Devices With Atomic Layer Deposited $HfTiO_x$ Nanolaminate. *IEEE electron device letters* **2013,** *34* (7), 867-869.
39.Fang, Z.; Wang, X. P.; Sohn, J.; Weng, B. B.; Zhang, Z. P.; Chen, Z. X.; Tang, Y. Z.; Lo, G.-Q.; Provine, J.; Wong, S. S., The role of Ti capping layer in HfO_x-based RRAM devices. *IEEE Electron Device Letters* **2014,** *35* (9), 912-914.
40.JDP, C.; AJ, R.; Boxford, W.; Moffitt, C.; Takahashi, K., Reduced preferential sputtering of TiO_2 using massive argon clusters. *Journal of surface analysis* **2014,** *20* (3), 211-215.
41.Végh, J., The Shirley background revised. *Journal of electron spectroscopy and related phenomena* **2006,** *151* (3), 159-164.
42.AGREATERMEASUREOFCONF, I., 1.888. KEITHLEY (US only).
43.Stathis, J. H.; DiMaria, D. In *Reliability projection for ultra-thin oxides at low voltage*, International Electron Devices Meeting 1998. Technical Digest (Cat. No. 98CH36217), IEEE: 1998; pp 167-170.
44.DiMaria, D.; Stathis, J., Ultimate limit for defect generation in ultra-thin silicon dioxide. *Applied physics letters* **1997,** *71* (22), 3230-3232.
45.Radu, R.; Pintilie, I.; Nistor, L.; Fretwurst, E.; Lindstroem, G.; Makarenko, L., Investigation of point and extended defects in electron irradiated silicon—Dependence on the particle energy. *Journal of Applied Physics* **2015,** *117* (16), 164503.
46.Sayan, S.; Croft, M.; Nguyen, N. V.; Emge, T.; Ehrstein, J.; Levin, I.; Suehle, J.; Bartynski, R. A.; Garfunkel, E. In *The Relation Between Crystalline Phase, Electronic Structure, and Dielectric Properties in High-K Gate Stacks*, AIP Conference Proceedings, American Institute of Physics: 2005; pp 92-101.
47.Sowinska, M.; Bertaud, T.; Walczyk, D.; Thiess, S.; Schubert, M. A.; Lukosius, M.; Drube, W.; Walczyk, C.; Schroeder, T., Hard x-ray photoelectron spectroscopy study of the electroforming in Ti/HfO_2-based resistive switching structures. *Applied Physics Letters* **2012,** *100* (23), 233509.
48.Triyoso, D.; Hegde, R.; Zollner, S.; Ramon, M.; Kalpat, S.; Gregory, R.; Wang, X.-D.; Jiang, J.; Raymond, M.; Rai, R., Impact of titanium addition on film characteristics of HfO_2 gate dielectrics deposited by atomic layer deposition. *Journal of applied physics* **2005,** *98* (5), 054104.
49.Wu, E. Y.; Suñé, J., Generalized hydrogen release-reaction model for the breakdown of modern gate dielectrics. *Journal of Applied Physics* **2013,** *114* (1), 014103.
50.Wu, E. Y., Facts and Myths of Dielectric Breakdown Processes—Part I: Statistics, Experimental, and Physical Acceleration Models. *IEEE Transactions on Electron Devices* **2019,** *66* (11), 4523-4534.
51.Zhao, L.; Clima, S.; Magyari-Köpe, B.; Jurczak, M.; Nishi, Y., Ab initio modeling of oxygen-vacancy formation in doped-HfO_x RRAM: Effects of oxide phases, stoichiometry, and dopant concentrations. *Applied Physics Letters* **2015,** *107* (1), 013504.
52.Hamer, P.; Nampalli, N.; Hameiri, Z.; Kim, M.; Chen, D.; Gorman, N.; Hallam, B.; Abbott, M.; Wenham, S., Boron-oxygen defect formation rates and activity at elevated temperatures. *Energy Procedia* **2016,** *92*, 791-800.
53.Chakrabarti, B., *Investigation of metal oxide dielectrics for non-volatile floating gate and resistance switching memory applications*. The University of Texas at Dallas: 2014.
54.Bersuker, G.; Veksler, D.; Nminibapiel, D. M.; Shrestha, P. R.; Campbell, J. P.; Ryan, J. T.; Baumgart, H.; Mason, M. S.; Cheung, K. P., Toward reliable RRAM performance: macro-and micro-analysis of operation processes. *Journal of Computational Electronics* **2017,** *16* (4), 1085-1094.

55.Hannula, M.; Ali-Löytty, H.; Lahtonen, K.; Sarlin, E.; Saari, J.; Valden, M., Improved stability of atomic layer deposited amorphous TiO_2 photoelectrode coatings by thermally induced oxygen defects. *Chemistry of Materials* **2018,** *30* (4), 1199-1208.
56.Wagner, C.; Naumkin, A.; Kraut-Vass, A.; Allison, J.; Powell, C.; Rumble Jr, J., NIST standard reference database 20, Version 3.4 (Web version). *National Institute of Standards and Technology: Gaithersburg, MD* **2003,** *20899*.